

A TWO-STAGE IMAGE SEGMENTATION METHOD FOR BLURRY IMAGES WITH POISSON OR MULTIPLICATIVE GAMMA NOISE

RAYMOND CHAN*, HONGFEI YANG†, AND TIEYONG ZENG‡

Abstract. In this paper, a two-stage method for segmenting blurry images in the presence of Poisson or multiplicative Gamma noise is proposed. The method is inspired by a previous work on two-stage segmentation and the usage of an I-divergence term to handle the noise. The first stage of our method is to find a smooth solution u to a convex variant of the Mumford-Shah model. A primal-dual algorithm is adopted to efficiently solve the minimization problem. We prove the convergence of the algorithm and the uniqueness of the solution u . Once u is obtained, then in the second stage, the segmentation is done by thresholding u into different phases. The thresholds can be given by the users or can be obtained automatically by using any clustering method. In our method, we can obtain any K -phase segmentation ($K \geq 2$) by choosing $(K - 1)$ thresholds after u is found. Changing K or the thresholds does not require u to be re-computed. Experimental results show that our two-stage method performs better than many standard two-phase or multi-phase segmentation methods for very general images, including anti-mass, tubular, MRI and low-light images.

Key words. Convexity, image segmentation, Gamma noise, multiplicative noise, primal-dual algorithm, total variation.

AMS subject classifications. 52A41, 65K10, 65K15, 90C30, 90C47.

1. Introduction. Image segmentation is an important task in image analysis and computer vision. It aims to separate objects of interest from each others or from the background, or to find boundaries of such objects. In [47, 48], Mumford and Shah introduced an energy minimization model that allows one to compute an optimal piecewise continuous or piecewise constant approximation u of a given image f . Since then, their model has been studied in depth in various aspects, e.g. the properties of minimizers [21], approximations and simplifications of their functional and its applications to the problem of image segmentation [1, 2, 13, 14, 15, 19, 29, 46].

Denote $\Omega \subset \mathbb{R}^2$ to be the image domain. More specifically, we assume Ω is bounded, open and connected, with Lipschitz boundary. Let $f : \Omega \rightarrow \mathbb{R}$ be a given gray scale image. In [47, 48], Mumford and Shah proposed to segment f by calculating an optimal approximation u of f and a decomposition

$$\Omega = \Omega_1 \cup \Omega_2 \cup \dots \cup \Omega_n \cup \Gamma$$

of the image domain such that the following requirements are satisfied: Ω_i 's are disjointly connected open subsets in Ω with Lipschitz boundaries, Γ is the collection of the boundaries of Ω_i 's and u varies smoothly in Ω_i . Then the functional E to be minimized for image segmentation is defined by [47, 48]

$$E(u, \Gamma) = \frac{\lambda}{2} \int_{\Omega} (f - u)^2 dx + \frac{\mu}{2} \int_{\Omega \setminus \Gamma} |\nabla u|^2 dx + \mathcal{H}^1(\Gamma), \quad (1.1)$$

* Department of Mathematics, The Chinese University of Hong Kong, Shatin, Hong Kong. Research is supported in part by HKRGC Grant No. CUHK400412, CUHK DAG 4053007, and CUHK FIS Grant 1902036. Email: rchan@math.cuhk.edu.hk.

† Department of Mathematics, The Chinese University of Hong Kong, Shatin, Hong Kong. Email: yanghongfei@cuhk.edu.hk.

‡ Department of Mathematics, Hong Kong Baptist University, Kowloon Tong, Hong Kong. Research is supported in part by the National Science Foundation of China (11271049), and HKRGC 211710, 211911 and RFGs of HKBU. Email: zeng@hkbu.edu.hk.

where \mathcal{H}^1 denotes the 1-dimensional Hausdorff measure in \mathbb{R}^2 .

Because (1.1) is nonconvex, it is very difficult to find or approximate its minimizer. Historically, there are two approaches to study the minimizer of (1.1). One is to approximate the functional by other functionals. In [1, 2], the authors approximated the functional (1.1) by elliptic functionals defined on Sobolev spaces. In [13, 14, 15, 29, 46], the authors approximated (1.1) by discrete functionals. Recently, a primal-dual algorithm based on convex relaxation for solving (1.1) was proposed in [50], which produces results independent of initializations.

Another approach is to simplify the functional (1.1). For example, if we restrict $\nabla u \equiv 0$ on $\Omega \setminus \Gamma$, then it results in a piecewise constant Mumford-Shah model. In [19], the method of active contours without edges (Chan-Vese model) for two-phase segmentation was introduced. For the works on the general piecewise constant Mumford-Shah model, see [36, 59, 60], etc. The main drawback of these methods is that they can easily get stuck in local minima. To overcome the problem, convex relaxation approaches [9, 17, 51], graph cut method [31] and fuzzy membership functions [39] were proposed.

In [11], the authors proposed a novel two-stage segmentation method. In the first stage, a smooth solution u is extracted from the given image f by minimizing the functional

$$E(u) = \int_{\Omega} |\nabla u| dx + \frac{\mu}{2} \int_{\Omega} |\nabla u|^2 dx + \frac{\lambda}{2} \int_{\Omega} (\mathcal{A}u - f)^2 dx. \quad (1.2)$$

Here \mathcal{A} is a blurring operator if the given image f is blurred or is the identity operator if there is no blur. In the second stage, a thresholding technique is adopted to segment the smooth solution u . This model has several advantages. The first one is the convexity of the functional (1.2), which, under mild conditions, guarantees a unique solution that is independent of initializations. The second one is that their model can handle multiphase segmentation efficiently. The third one is that the thresholding is independent from the process of finding u . Users therefore can employ an automated clustering method to find the threshold, or they can try different phases and thresholds to get a satisfactory segmentation—all without recalculating u . One interesting aspect of the model (1.2) is that it closely links three major components of image processing together: denoising, deblurring and segmentation. In fact, model (1.2) has been employed in [33] as an image restoration model.

Bearing in mind the maximum-a-posteriori (MAP) approach, the model in [11] with the data fitting term $\int_{\Omega} (\mathcal{A}u - f)^2 dx$ is only suitable for images degraded by additive Gaussian noise. There are in fact many competing methods for segmenting images corrupted by Gaussian noise, see for instance [5, 11, 19, 22, 35, 39, 51, 54, 62, 63]. However as far as we know, there are only few works on segmenting images corrupted by Poisson or multiplicative Gamma noise. In [20, 45, 52], the authors proposed snake-based segmentation methods adapted to physical noise of the exponential family (Gaussian, Gamma, Rayleigh, Poisson, etc). In [28], a minimum description length (MDL) criterion is proposed to image segmentation with speckle, Poisson or Bernoulli noise. In [55], the authors proposed a general segmentation framework, and studied additive Gaussian noise, Poisson noise and multiplicative speckle noise. To our knowledge, there are no papers on the segmentation of blurry images corrupted by Poisson or multiplicative Gamma noise.

Here in this paper, inspired by the works from [11] and [58], we propose a two-stage convex segmentation method to segment blurry images degraded by Poisson or multiplicative Gamma noise. In the first stage of our method, we extract a smooth

image u from the given image f . In the second stage we threshold u to reveal different segmentation features. To find u , we minimize the functional

$$\int_{\Omega} |\nabla u| dx + \frac{\mu}{2} \int_{\Omega} |\nabla u|^2 dx + \lambda \int_{\Omega} (\mathcal{A}u - f \log \mathcal{A}u) dx, \quad (1.3)$$

which is different from the first stage in [11] (i.e. equation (1.2)) by the data fitting term. As observed in [4], the data fitting term $h(u) := \int_{\Omega} (u - f \log u) dx$ is deduced by MAP probability density $p(u|f)$ when image f is corrupted by Poisson noise. In [58], the authors used $h(u)$ as the data fitting term, and proposed a new model for denoising multiplicative Gamma noise. They gave both theoretical explanations and numerical experiments to justify why $h(u)$ is also suitable to handle multiplicative Gamma noise. Therefore, it is natural for us to introduce the data fitting term $h(u)$ to our two-stage segmentation model when the image is blurry, and corrupted by either Poisson or multiplicative Gamma noise.

We will prove that the minimization of the functional (1.3) has a unique solution u which can be solved efficiently by popular algorithms such as the split-Bregman [30] or the Chambolle-Pock algorithm [16, 50]. One nice aspect of our method is that there is no need to re-compute u if we have to change the threshold in the second stage to reveal different features in the image. Another nice aspect is that there is no need to specify the number of phases before u is found. We can obtain any K -phase segmentation ($K \geq 2$) by choosing $(K-1)$ thresholds after u is computed in the first stage. In contrast, multiphase methods such as those in [5, 10, 25, 38, 39, 40, 41, 51, 56, 62] require K to be given first; and if K changes, the minimization problem has to be solved all over again.

The rest of this paper is organized as follows. In Section 2, we briefly review the model in [11] and its properties, since it shares a similar structure with our model. In Section 3, we introduce our method, and show that the minimization model has a unique solution. In Section 4, we give the detailed implementation of our method, and show that the resulting algorithm converges. In Section 5, we provide numerical results to verify the effectiveness of our method. In the last section, we conclude our discussion, and point out possible improvements.

2. Review on the model in [11]. Since the model in [11] shares a similar structure with our method, we briefly review it here. The model has two stages. In the first stage, one solves the minimization problem:

$$\inf_{u \in W^{1,2}(\Omega)} E(u) = \inf_{u \in W^{1,2}(\Omega)} \left\{ \int_{\Omega} |\nabla u| dx + \frac{\mu}{2} \int_{\Omega} |\nabla u|^2 dx + \frac{\lambda}{2} \int_{\Omega} (f - \mathcal{A}u)^2 dx \right\}, \quad (2.1)$$

where μ and λ are positive parameters, \mathcal{A} is a given blurring operator, and f is the given image. After obtaining u , which is a smoothed version of f , one segments u by a proper thresholding method in the second stage.

This two stage model is based on the Mumford-Shah model, and it is inspired by the following observation: one can obtain a good restoration of a binary image by thresholding its smoothed version with a proper threshold, see [11]. Assume that Γ is a Jordan curve with measure 0. Let $\Sigma = \overline{\text{Inside}(\Gamma)}$, then $\Gamma = \partial\Sigma$. The objective functional in the Mumford-Shah model (1.1) can be written as:

$$\begin{aligned} \tilde{E}(\Sigma, g_1, g_2) &= \frac{\lambda}{2} \int_{\Sigma \setminus \Gamma} (f - g_1)^2 dx + \frac{\mu}{2} \int_{\Sigma \setminus \Gamma} |\nabla g_1|^2 dx + \frac{\lambda}{2} \int_{\Omega \setminus \Sigma} (f - g_2)^2 dx \\ &\quad + \frac{\mu}{2} \int_{\Omega \setminus \Sigma} |\nabla g_2|^2 dx + \text{Length}(\Gamma), \end{aligned} \quad (2.2)$$

where g_1 and g_2 are defined on $\Sigma \setminus \Gamma$ and $\Omega \setminus \Sigma$ respectively. Inspired by the proof of Theorem 2 in [17], the authors in [11] then proved that a global minimizer of (2.2) with fixed g_1 and g_2 can be found by carrying out the following minimization

$$\min_{0 \leq u \leq 1} \left\{ \int_{\Omega} |\nabla u| dx + \frac{1}{2} \int_{\Omega} \{ \lambda(f - g_1)^2 + \mu |\nabla g_1|^2 - \lambda(f - g_2)^2 - \mu |\nabla g_2|^2 \} u(x) dx \right\}, \quad (2.3)$$

and setting $\Sigma = \{x : u(x) \geq \rho\}$ for $\rho \in [0, 1]$ a.e. In this way, the authors replaced the Length(Γ) term by a convex integral term $\int_{\Omega} |\nabla u| dx$, and proposed the first stage as (2.1).

After u is obtained, the authors in [11] proposed several ways to determine proper threshold(s) ρ 's. For two-phase segmentations, one can set ρ to be the mean of u , or the user can try different values of ρ to get the best result. For multi-phase segmentation, one can use clustering techniques to determine values of ρ 's automatically. One such technique is the K-means method [32, 34, 43], and the authors in [11] used it in their numerical experiments for both two-phase and multi-phase segmentation. Note that changing ρ 's does not require u to be re-computed.

3. A two-stage segmentation method for Poisson or multiplicative Gamma noise. Let us first introduce the Poisson noise and the multiplicative Gamma noise. For the Poisson noise, for each pixel $x \in \Omega$ we assume $f(x)$ is a random variable following the Poisson distribution with mean $u(x)$, i.e., its probability mass function is:

$$p_{f(x)}(n; u(x)) = \frac{(u(x))^n e^{-u(x)}}{n!}.$$

In this case, we say that f is corrupted by Poisson noise.

For the Gamma noise, suppose that for each pixel $x \in \Omega$ the random variable $\eta(x)$ follows the Gamma distribution, i.e., its probability density function is:

$$p_{\eta(x)}(y; \theta, K) = \frac{1}{\theta^K \Gamma(K)} y^{K-1} e^{-\frac{y}{\theta}} \text{ for } y \geq 0, \quad (3.1)$$

where Γ is the usual Gamma-function, θ and K denote the scale and shape parameters in the Gamma distribution respectively. Notice that, the mean of $\eta(x)$ is $K\theta$, and the variance of $\eta(x)$ is $K\theta^2$. For multiplicative noise, we assume in general that the mean of $\eta(x)$ equals 1, see [4, 24]. Then we have $K\theta = 1$ and its variance is $1/K$. We assume the degraded image is $f(x) = u(x) \cdot \eta(x)$, and say that f is corrupted by multiplicative Gamma noise.

Our method is inspired by the following observations. Suppose f is the given image with noise following a certain statistical distribution. Then based on MAP approach, restoring the image u is equivalent to maximizing the probability $p(u|f)$. Assume the prior distribution of u is given by

$$p(u) \propto \exp(-\beta \int_{\Omega} |\nabla u| dx),$$

where β is a parameter. If the noise follows the Poisson distribution, then maximizing $p(u|f)$ corresponds to minimizing the functional

$$\int_{\Omega} (u - f \log u) dx + \beta \int_{\Omega} |\nabla u| dx, \quad (3.2)$$

see [37]. If the noise is multiplicative following the Gamma distribution, then maximizing $p(u|f)$ corresponds to minimizing the functional

$$\int_{\Omega} \frac{f}{u} + \log u dx + \beta \int_{\Omega} |\nabla u| dx, \quad (3.3)$$

see [4]. However, it is observed in the numerical examples in [4, 57] that for the denoising model (3.3) the noise survives much longer at low image values if we increase the regularization parameter. Therefore, in [57] the authors suggested to take $w = \log u$ and change the objective functional (3.3) to

$$\int_{\Omega} f e^{-w} + w dx + \beta \int_{\Omega} |\nabla w| dx. \quad (3.4)$$

In [58], the authors employed the objective functional (3.2) to restore images corrupted by multiplicative Gamma noise and they justified their selection as follows. First, the gradients of the data fitting term in (3.2) and (3.4) are the same if we use again the relation $w = \log u$. Second, both (3.2) and (3.4) have the same minimizer. Numerical results from [58] also suggests that the functional (3.2) is effective in dealing with multiplicative Gamma noise. Therefore, if we want to segment images corrupted by Poisson noise or multiplicative Gamma noise, it is natural to change the data fitting term $\int_{\Omega} (f - \mathcal{A}u)^2 dx$ in model (2.1) to $\int_{\Omega} (\mathcal{A}u - f \log \mathcal{A}u) dx$. Then we have the following minimization problem:

$$\inf_{u \in W^{1,2}(\Omega)} E(u) = \inf_{u \in W^{1,2}(\Omega)} \left\{ \int_{\Omega} |\nabla u| dx + \frac{\mu}{2} \int_{\Omega} |\nabla u|^2 dx + \lambda \int_{\Omega} (\mathcal{A}u - f \log \mathcal{A}u) dx \right\}. \quad (3.5)$$

After obtaining u from the minimization problem (3.5), we adopt the same approach as in [11] to get a segmentation of u in the second stage. More precisely, we can try different thresholds to get the best segmentation result, or we can use the K-means clustering method to get an automatic algorithm. Here we stress again that there is no need to re-compute u if we change the number of phases K or the thresholds ρ 's.

In the following, we study the existence and uniqueness of the solution of (3.5). Since most digital images have predefined ranges, it is natural to assume $f \in L^{\infty}(\Omega)$, and we further assume $\inf f > 0$. We first study the case when the continuous linear operator \mathcal{A} is the identity operator, i.e.,

$$\inf_{u \in W^{1,2}(\Omega)} E(u) = \inf_{u \in W^{1,2}(\Omega)} \left\{ \int_{\Omega} |\nabla u| dx + \frac{\mu}{2} \int_{\Omega} |\nabla u|^2 dx + \lambda \int_{\Omega} (u - f \log u) dx \right\}. \quad (3.6)$$

THEOREM 3.1. *Let Ω be a bounded connected open subset of \mathbb{R}^2 with a Lipschitz boundary. Let $f \in L^{\infty}(\Omega)$ with $\inf f > 0$. Then (3.6) has a unique minimizer $u \in W^{1,2}(\Omega)$ satisfying $0 < \inf f \leq u \leq \sup f$.*

Proof. For any function $g \in W^{1,2}(\Omega)$, define $g^+ = \max(g, 0)$ and $g^- = -\min(g, 0)$. Then we have $g = g^+ - g^-$. It is clear that $\{u - f \log u\}$ takes its minimum at $u = f$, and it tends to positive infinite when $u \rightarrow \infty$, so $E(u)$ is bounded from below. By taking $u \equiv 1 \in W^{1,2}(\Omega)$, we see $E(u) < \infty$, so $E(u)$ is proper. Let $\{u_n\}$ be a minimizing sequence. Then there exists an $M > 0$ such that $E(u_n) \leq M$ for all $n \in \mathbb{N}$. Therefore we have

$$M \geq \int_{\Omega} (u_n - f \log u_n) dx \geq - \int_{\Omega} (u_n - f \log u_n)^- dx,$$

for all $n \in \mathbb{N}$. Since $(u_n - f \log u_n)^-$ is uniformly bounded from above by $|f - f \log f| < \infty$, we conclude that $\int_{\Omega} (u_n - f \log u_n) dx$ is uniformly bounded from below. From this and the uniform boundedness of $E(u_n)$, it is clear that both $\|\nabla u_n\|_1 = \int_{\Omega} |\nabla u_n| dx$ and $\|\nabla u_n\|_2 = (\int_{\Omega} |\nabla u_n|^2 dx)^{\frac{1}{2}}$ are uniformly bounded.

Since $f \in L^{\infty}(\Omega)$, f is bounded from above. Thus for all $y \in \Omega$, there exists a $u_0 > 0$ such that $2(x - f(y) \log x) \geq x$ for $x \geq u_0$. Therefore we conclude that

$$\begin{aligned} \int_{\Omega} |u_n| dx &\leq \int_{\Omega} \max \{2(u_n - f \log u_n), u_0\} dx \leq 2 \int_{\Omega} (u_n - f \log u_n)^+ dx + \int_{\Omega} u_0 dx \\ &\leq 2 \int_{\Omega} (u_n - f \log u_n) dx + 2 \int_{\Omega} (u_n - f \log u_n)^- dx + \int_{\Omega} u_0 dx < \infty, \end{aligned}$$

for all $n \in \mathbb{N}$. Thus we have proved that $\|u_n\|_1$ is uniformly bounded.

From the Poincaré inequality [26], we have

$$\|u_n - m_{\Omega}(u_n)\|_2 \leq C \|\nabla u_n\|_2,$$

where $m_{\Omega}(u_n) = \frac{1}{|\Omega|} \int_{\Omega} u_n dx$, $|\Omega|$ is the Lebesgue measure of Ω and C is a constant related to Ω . Thus $\|u_n - m_{\Omega}(u_n)\|_2$ is uniformly bounded. Notice that we have already proved that $\|u_n\|_1$ is uniformly bounded. From this we conclude that

$$\begin{aligned} \|u_n\|_2 &\leq \|u_n - m_{\Omega}(u_n)\|_2 + \|m_{\Omega}(u_n)\|_2 \\ &\leq \|u_n - m_{\Omega}(u_n)\|_2 + \|u_n\|_1 \end{aligned}$$

is uniformly bounded.

Therefore, up to a subsequence, u_n converges strongly in $W^{1,2}(\Omega)$ to some u^* , and ∇u_n converges weakly as a measure to ∇u^* . By the lower semi-continuity of $E(u)$, we have $E(\liminf_{n \rightarrow \infty} u_n) \leq \liminf_{n \rightarrow \infty} E(u_n)$, and therefore u^* is a solution to (3.6).

Let $\alpha = \inf f$ and $\beta = \sup f$. By Proposition 15 in [21], both $\min(u^*, \beta)$ and $\max(u^*, \alpha)$ are members of $W^{1,2}(\Omega)$, and

$$|\nabla(\min(u^*, \beta))| \leq |\nabla u^*|, \quad |\nabla(\max(u^*, \alpha))| \leq |\nabla u^*|.$$

Then following the same arguments as in Theorem 4.1 in [4], we have $\alpha \leq u^* \leq \beta$.

The uniqueness of the minimizer follows from the strict convexity of the objective functional in (3.6). \square

Next we study the case when \mathcal{A} is a blurring operator. We show that our main model (3.5) has a unique solution if $\text{Ker}(\mathcal{A}) \cap \text{Ker}(\nabla) = \{0\}$, where $\text{Ker}(\cdot)$ represents the kernel. This condition says that $\mathcal{A}1 \neq 0$. In real applications, the blurring operator is a convolution with positive kernel, so the condition $\text{Ker}(\mathcal{A}) \cap \text{Ker}(\nabla) = \{0\}$ is satisfied.

THEOREM 3.2. *Let Ω be a bounded connected open subset of \mathbb{R}^2 with a Lipschitz boundary. Let $f \in L^{\infty}(\Omega)$ with $\inf f > 0$, and let \mathcal{A} be a continuous linear operator from $W^{1,2}(\Omega)$ to itself. Assume $\text{Ker}(\mathcal{A}) \cap \text{Ker}(\nabla) = \{0\}$, then (3.5) has a unique minimizer $u \in W^{1,2}(\Omega)$.*

Proof. Let $\{u_n\}$ be a minimizing sequence. Then as argued in the proof of Theorem 3.1, it is clear that $\|\nabla u_n\|_1$, $\|\nabla u_n\|_2$ and $\|\mathcal{A}u_n\|_1$ are all uniformly bounded. By the Poincaré inequality, we have

$$\|u_n - m_{\Omega}(u_n)\|_1 \leq C_1 \|\nabla u_n\|_1,$$

for some constant C_1 . Thus $\|u_n - m_\Omega(u_n)\|_1$ is uniformly bounded. We have

$$\begin{aligned} |m_\Omega(u_n)|\|\mathcal{A}1\|_1 &= \|\mathcal{A}(m_\Omega(u_n)1)\|_1 \\ &= \|\mathcal{A}(m_\Omega(u_n) - u_n) + \mathcal{A}u_n\|_1 \\ &\leq \|\mathcal{A}(m_\Omega(u_n) - u_n)\|_1 + \|\mathcal{A}u_n\|_1. \end{aligned}$$

Since $\|u_n - m_\Omega(u_n)\|_1$ is uniformly bounded, \mathcal{A} is continuous, and $\mathcal{A}1 \neq 0$, we see that $m_\Omega(u_n)$ is uniformly bounded. By the Poincaré inequality again, we see that

$$\|u_n - m_\Omega(u_n)\|_2 \leq C_2 \|\nabla u_n\|_2,$$

for some constant C_2 . Thus $\|u_n\|_2 \leq \|u_n - m_\Omega(u_n)\|_2 + \|m_\Omega(u_n)\|_2$ is uniformly bounded. Therefore, up to a subsequence, u_n converges strongly in $W^{1,2}(\Omega)$ to some u^* , and ∇u_n converges weakly as a measure to ∇u^* . Then from the lower semi-continuity of $E(u)$, we conclude that u^* is a minimizer of (3.5). Notice that $\mathcal{A}u - f \log \mathcal{A}u$ is strictly convex in $\mathcal{A}u$. Thus the uniqueness of the minimizer follows from the same argument as in Theorem 2.4 [11].

□

4. The primal-dual algorithm for solving (3.5). Because of the convexity of the minimization problem (3.5), many methods can be used to solve it. For example, the primal-dual algorithms [12, 16, 18, 65], which can be easily adapted to a number of non-smooth convex optimization problems and is easy to implement; and the alternating direction method with multipliers (ADMM) [8, 27], which is convergent and is well-suited to large-scale convex problems. Recently, several specific algorithms for solving TV regularized problems have been proposed: the split-Bregman algorithm [30], which is closely connected to the ADMM method, and has fast convergence for TV regularized problems; the Chambolle-Pock algorithm [16], which solves a general saddle-point problem based on primal-dual approach, is fast, flexible, and there is a known convergent rate. In this paper, we employ the Chambolle-Pock algorithm to solve the minimization problem (3.5).

We now derive the discrete version of (3.5). We keep the same notations from the continuous context for the sake of simplicity. Suppose that the original image $f \in \mathbb{R}^{mn \times 1}$ is obtained from a two-dimensional pixel-array (size $m \times n$) by concatenation in the usual columnwise fashion, and $f \in [1, 255]$ (we set $f = \max(f, 1)$). Define the function $G : \mathbb{R}^{mn \times 1} \rightarrow \mathbb{R}$ as

$$G(v) = \sum_i (v_i - f_i \log v_i), \quad v > 0.$$

The discrete gradient operator is the map $\nabla : \mathbb{R}^{mn \times 1} \rightarrow \mathbb{R}^{2mn \times 1}$ defined as:

$$\nabla u = \begin{pmatrix} \nabla_x u \\ \nabla_y u \end{pmatrix},$$

with ∇_x and ∇_y corresponding to the discrete derivative operators in the x -direction and y -direction respectively. In our numerical experiments, ∇_x and ∇_y are obtained by applying finite difference approximations to the derivatives with symmetric boundary conditions in the respective coordinate directions. In addition, $\|\nabla u\|_1$ denotes the discrete total variation of u , i.e.,

$$\|\nabla u\|_1 = \sum_i \sqrt{(\nabla_x u)_i^2 + (\nabla_y u)_i^2}.$$

Then the discrete version of the minimization problem (3.5) is

$$\min_u E(u) = \min_u \left\{ \|\nabla u\|_1 + \frac{\mu}{2} \|\nabla u\|_2^2 + \lambda G(Au) \right\}, \quad (4.1)$$

where $A \in \mathbb{R}^{mn \times mn}$ is the blurring matrix from the discretization of \mathcal{A} . In the numerical tests, we impose symmetric boundary conditions on A too.

Next, we introduce new variables $v \in \mathbb{R}^{2mn \times 1}$ and $w \in \mathbb{R}^{mn \times 1}$, and reformulate the minimization problem (4.1) as the following constrained optimization problem:

$$\min_{u,v,w} \left\{ \|v\|_1 + \frac{\mu}{2} \|v\|_2^2 + \lambda G(w) \right\} \quad \text{s.t. } v = \nabla u, w = Au. \quad (4.2)$$

To employ the Chambolle-Pock algorithm, we consider the following primal-dual optimization problem:

$$\min_{u,v,w} \max_{p,q} \left\{ \|v\|_1 + \frac{\mu}{2} \|v\|_2^2 + \lambda G(w) + \langle v - \nabla u, p \rangle + \langle w - Au, q \rangle \right\}. \quad (4.3)$$

Then the Chambolle-Pock algorithm is defined through the iterations:

$$p^{(k+1)} = \arg \max_p \left\{ \langle \bar{v}^{(k)} - \nabla \bar{u}^{(k)}, p \rangle - \frac{1}{2\sigma} \|p - p^{(k)}\|_2^2 \right\}, \quad (4.4)$$

$$q^{(k+1)} = \arg \min_q \left\{ \langle \bar{w}^{(k)} - A\bar{u}^{(k)}, q \rangle - \frac{1}{2\sigma} \|q - q^{(k)}\|_2^2 \right\}, \quad (4.5)$$

$$u^{(k+1)} = \arg \min_u \left\{ -\langle \nabla u, p^{(k+1)} \rangle - \langle Au, q^{(k+1)} \rangle + \frac{1}{2\tau} \|u - u^{(k)}\|_2^2 \right\}, \quad (4.6)$$

$$v^{(k+1)} = \arg \min_v \left\{ \|v\|_1 + \frac{\mu}{2} \|v\|_2^2 + \langle v, p^{(k+1)} \rangle + \frac{1}{2\tau} \|v - v^{(k)}\|_2^2 \right\}, \quad (4.7)$$

$$w^{(k+1)} = \arg \min_w \left\{ \lambda G(w) + \langle w, q^{(k+1)} \rangle + \frac{1}{2\tau} \|w - w^{(k)}\|_2^2 \right\}, \quad (4.8)$$

$$\bar{u}^{(k+1)} = 2u^{(k+1)} - u^{(k)}, \quad (4.9)$$

$$\bar{v}^{(k+1)} = 2v^{(k+1)} - v^{(k)}, \quad (4.10)$$

$$\bar{w}^{(k+1)} = 2w^{(k+1)} - w^{(k)}. \quad (4.11)$$

Since the objective functions (4.4)–(4.6) are quadratic, the update of p , q and u can be computed efficiently:

$$p^{(k+1)} = \sigma(\bar{v}^{(k)} - \nabla \bar{u}^{(k)}) + p^{(k)}, \quad (4.12)$$

$$q^{(k+1)} = \sigma(\bar{w}^{(k)} - A\bar{u}^{(k)}) + q^{(k)}, \quad (4.13)$$

$$u^{(k+1)} = u^{(k)} + \tau(A^T q^{(k+1)} - \text{div} p^{(k+1)}). \quad (4.14)$$

The solution of (4.7) can be easily obtained by applying the soft thresholding operator. Denote $t^{(k)} = \frac{\tau}{\mu\tau+1}(\frac{1}{\tau}v^{(k)} - p^{(k+1)})$, we have

$$v^{(k+1)} = \max \left\{ \|t^{(k)}\|_1 - \frac{\tau}{\mu\tau+1}, 0 \right\} \cdot \frac{t^{(k)}}{\|t^{(k)}\|_1}. \quad (4.15)$$

The optimality condition for (4.8) gives the quadratic equation

$$w^2 + (\tau(\lambda + q^{(k+1)}) - w^{(k)})w - \lambda\tau f = 0.$$

Its solution is given by

$$w = \frac{w^{(k)} - \tau(q^{(k+1)} + \lambda) + [(\tau(\lambda + q^{(k+1)}) - w^{(k)})^2 + 4\tau\lambda f]^{1/2}}{2}. \quad (4.16)$$

The following algorithm summarizes the procedures to solve the optimization problem (4.1).

Algorithm 1: Solving (4.1) by the Chambolle-Pock algorithm

-
1. Initialize: $p^{(0)} = 0, u^{(0)} = \bar{u}^{(0)} = f, v^{(0)} = \bar{v}^{(0)} = \nabla f, w^{(0)} = \bar{w}^{(0)} = Au^{(0)}$.
 2. Do $k = 0, 1, \dots$, until $\frac{\|u^{(k)} - u^{(k+1)}\|}{\|u^{(k+1)}\|} < \epsilon$
 - (a) Compute $p^{(k+1)}$ by (4.12).
 - (b) Compute $q^{(k+1)}$ by (4.13).
 - (c) Compute $u^{(k+1)}$ by (4.14).
 - (d) Compute $v^{(k+1)}$ by (4.15).
 - (e) Compute $w^{(k+1)}$ by (4.16).
 - (f) Update $\bar{u}^{(k+1)}, \bar{v}^{(k+1)}$ and $\bar{w}^{(k+1)}$ by (4.9), (4.10) and (4.11).
 3. Output: u .
-

Note that if A is the identity operator, there is no need to introduce w and q , and the algorithm can be simplified accordingly.

In the following, we discuss the existence of solution to (4.3) and the convergence of Algorithm 1. Define

$$K = \begin{pmatrix} -\nabla & I & 0 \\ -A & 0 & I \end{pmatrix}, \quad x = \begin{pmatrix} u \\ v \\ w \end{pmatrix}, \quad \bar{x} = \begin{pmatrix} \bar{u} \\ \bar{v} \\ \bar{w} \end{pmatrix}, \quad y = \begin{pmatrix} p \\ q \end{pmatrix}.$$

Then (4.3) is equivalent to

$$\min_x \max_y \{H(x) + \langle Kx, y \rangle\}, \quad (4.17)$$

where $H(x) = \|v\|_1 + \frac{\mu}{2}\|v\|_2^2 + \lambda G(w)$. First we note that

PROPOSITION 4.1. *The saddle point set of (4.17) is nonempty.*

The proof follows the same arguments as in Proposition 2 [42].

Next we show that Algorithm 1 converges.

PROPOSITION 4.2. *Let $\|K\|_2$ be the operator 2-norm of K and $(x^{(n)}, \bar{x}^{(n)}, y^{(n)})$ be defined by Algorithm 1. If we choose τ and σ such that $\tau\sigma < 1/\|K\|_2^2$, then $(x^{(n)}, y^{(n)})$ converges to a saddle point (x^*, y^*) of (4.17).*

The proposition is a special case of Theorem 1 in [16]. We remark that for the limiting point $(x^*, y^*) = (u^*, v^*, w^*, p^*, q^*)$, the u^* will be the unique solution of (4.1) that we seek. To see that, we first observe that (4.17) is the primal-dual formulation of

$$\min_x \{\iota(Kx) + H(x)\}, \quad (4.18)$$

where ι is the indicator function of the set $\{0\}$, see [16]. Clearly, by the definition of K and H , (4.18) is exact the same as (4.2). Since (4.1) has a unique solution (under the assumption that $\text{Ker}(A) \cap \text{Ker}(\nabla) = \{0\}$) and that $v := \nabla u$ and $w := Au$ (see (4.2)), we see that (4.18) has a unique solution too. By Proposition 3.1 of [23], if (x^*, y^*) is a saddle point of (4.17), then x^* is a solution of (4.18), and x^* is therefore unique.

Finally we give an estimate of $\|K\|_2$.

PROPOSITION 4.3. Denote $\alpha = \sqrt{\|\nabla\|_2^2 + \|A\|_2^2}$. Then $\|K\|_2 < \sqrt{\alpha^2 + 1}$.

Proof. To get a bound for the operator K , we have

$$\begin{aligned} \|Kx\|_2 &= \left\| \begin{pmatrix} -\nabla u + v \\ -Au + w \end{pmatrix} \right\|_2 \\ &\leq \left\| \begin{pmatrix} -\nabla u \\ -Au \end{pmatrix} \right\|_2 + \left\| \begin{pmatrix} v \\ w \end{pmatrix} \right\|_2 \\ &= \sqrt{\|\nabla u\|_2^2 + \|Au\|_2^2} + \left\| \begin{pmatrix} v \\ w \end{pmatrix} \right\|_2 \\ &\leq \sqrt{\|\nabla\|_2^2 + \|A\|_2^2} \|u\|_2 + \left\| \begin{pmatrix} v \\ w \end{pmatrix} \right\|_2. \end{aligned} \quad (4.19)$$

When $\|x\|_2 = 1$, that is $\|u\|_2^2 + \left\| \begin{pmatrix} v \\ w \end{pmatrix} \right\|_2^2 = 1$, we have

$$\begin{aligned} \|Kx\|_2 &\leq \alpha \|u\|_2 + \left\| \begin{pmatrix} v \\ w \end{pmatrix} \right\|_2 \\ &\leq \sqrt{\alpha^2 + 1} \cdot \sqrt{\|u\|_2^2 + \left\| \begin{pmatrix} v \\ w \end{pmatrix} \right\|_2^2} \\ &= \sqrt{\alpha^2 + 1}. \end{aligned} \quad (4.20)$$

Thus $\|K\|_2 \leq \sqrt{\alpha^2 + 1}$. However, we claim that the equality can not be achieved.

To see this, (4.20) is an equality if and only if $\|u\|_2 = \frac{\alpha}{\sqrt{\alpha^2+1}}$ and $\left\| \begin{pmatrix} v \\ w \end{pmatrix} \right\|_2 = \frac{1}{\sqrt{\alpha^2+1}}$.

In this case, $\|u\|_2 < 1$, and (4.19) becomes a strict inequality. \square

Since $\|\nabla\|_2 \leq 8$ (see [12]) and $\|A\|_2 \leq 1$ (see [42]), we conclude that if $\tau\sigma \leq 0.1$, the Algorithm 1 converges.

Let us remark that the above numerical scheme can be applied to handle the following problem:

$$\min_x \sum_{i=1}^n f_i(K_i x),$$

where for any i , K_i is bounded linear operator from \mathbb{R}^p to some \mathbb{R}^{m_i} and f_i is proper convex function. Indeed, we can rewrite the above problem as the following equivalent

min-max problem:

$$\max_{y_1, \dots, y_n} \min_{x, w_1, \dots, w_n} \left\{ \sum_{i=1}^n f_i(w_i) + \sum_{i=1}^n \langle w_i - K_i x, y_i \rangle \right\},$$

or

$$\max_Y \min_X \{f(X) + \langle KX, Y \rangle\}, \quad (4.21)$$

where $X = (x, w_1, \dots, w_n)^T$, $Y = (y_1, \dots, y_n)^T$, $f(X) := \sum_{i=1}^n f_i(w_i)$ and

$$K := \begin{pmatrix} -K_1 & I & 0 & \dots & 0 \\ -K_2 & 0 & I & \dots & 0 \\ & \dots & & & \\ -K_n & \dots & 0 & 0 & I \end{pmatrix}.$$

Readily, we can prove that $\|K\|_2 \leq \sqrt{1 + \sum_{i=1}^n \|K_i\|_2^2}$. Now, we can applied the Chambolle-Pock algorithm on (4.21).

5. Numerical experiments. In this section, we compare our method with other segmentation methods. To standardize the experiments, all test images have the range [1, 255] (we set $f = \max(f, 1)$) and we always set the mean $K\theta$ of the Gamma distribution to 1, see (3.1).

As far as we know, there are no papers on segmenting blurry images with either Poisson or multiplicative Gamma noise. The most recent paper [55] considered 2-phase segmentation with additive Gaussian noise, Poisson noise or multiplicative speckle noise, but with no blur. We will compare this method with ours. Besides, to be more comprehensive, we will compare with methods in [22, 39, 62, 63] which are effective segmentation methods for Gaussian noise proposed after 2010. For fair comparisons, we apply the Anscombe transformation to the test images before the implementation of the methods [22, 39, 62, 63]. Recall that the Anscombe transformation is defined by $f \rightarrow 2\sqrt{f + \frac{3}{8}}$, see [3]. Anscombe transformation can stabilize variance, and it has been used in the removal of Poisson noise, see [44].

We note that method [55] is a region-based variational segmentation framework. It is not convex and the segmentation results depend on initializations. Method [63] uses the continuous max-flow algorithm in [61] and a mimetic finite-difference discretization method [64] to solve the 2D continuous min-cut problem. Method [62] uses the same algorithm and method to solve the 2D continuous min-cut problem with multiple labels. Method [22] is based on tight frames and method [39] is based on fuzzy region competitions. Notice that we can not obtain the codes from authors in [55], so we coded the algorithm by our own. For the methods [22, 39, 62, 63], the codes are from the authors.

In our method, we put $\tau = 4$ and $\sigma = 0.025$ for a fast and stable implementation of Algorithm 1, see the remark after Proposition 4.3. For images with no blur, we terminate the iteration in Algorithm 1 when $\frac{\|u^{(k)} - u^{(k+1)}\|}{\|u^{(k+1)}\|} < 10^{-3}$, or the maximum iteration number 600 is reached. For images with blur, we terminate the iteration in Algorithm 1 when $\frac{\|u^{(k)} - u^{(k+1)}\|}{\|u^{(k+1)}\|} < 10^{-4}$, or the maximum iteration number 600 is reached. After we get u in (3.5), we choose threshold(s) to segment u . The thresholds are chosen by two methods. The first one is to use MATLAB K-means function

“KMEANS”. This provides an automatic segmentation process. The second method is to choose the threshold manually to produce good segmentation results. We use ρ^K to denote the thresholds obtained from the “KMEANS” command and ρ^U the thresholds chosen by us. Since u is calculated prior to the choosing of the number of phases and the thresholds, users can try different number of phases and thresholds without re-computing u .

For all the segmentation methods used in this section, we tuned the parameters in the experiments to achieve the best visual results. The boundaries of the results are superimposed on the given images for comparison. All the numerical experiments were run on a PC with 2.4GHz CPU, 4GB RAM and MATLAB 7.13 (R2011b).

5.1. Two-phase segmentation. In this subsection, we compare our method with the two-phase segmentation methods proposed in [22, 55, 63].

Example 5.1 (Poisson noise): Figure 5.1(a) is the original image “Boat”. This image is difficult to segment because of the inhomogeneity of the light: the brightness of the water varies with the top corners being darker, and the boat has both dark and light parts. We corrupted it with Poisson noise to make the segmentation more challenging, see Figure 5.1(b). Figure 5.1(f) is the solution u of (3.5) using $\lambda = 1$ and $\mu = 0.05$, and (g) is our segmentation result with threshold $\rho^K = 142.13$. It can be seen that our method segmented the body and the reflection of the boat successfully. Figure 5.1(c) from the method in [63] included the water of the top corners as part of the segmented object. Figure 5.1(d) from the method in [22] failed to segment the body and the reflection of the boat as a whole. Figure 5.1(e) of method [55] produced a segmentation similar to our result.

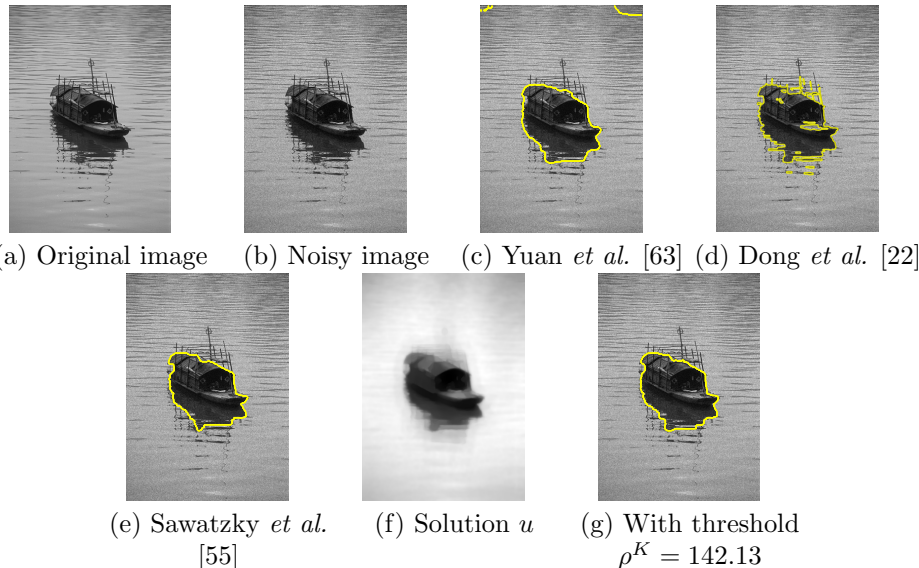


FIG. 5.1. (a) Original “Boat” image (450×321 pixels), (b) image corrupted by Poisson noise (c) Yuan *et al.* [63], (d) Dong *et al.* [22], (e) Sawatzky *et al.* [55], (f) solution u from (3.5) with $\lambda = 1$ and $\mu = 0.05$, (g) u threshold by $\rho^K = 142.13$.

Example 5.2 (Multiplicative Gamma noise): Figure 5.2(a) is the original “Anti-mass” image. We corrupt it by multiplicative Gamma noise with $K = 10$ to obtain Figure 5.2(b). The bright object in the image (the continental US) does not have a

clear cut boundary, and there are many tiny holes in the object, which all make it challenging to produce a good segmentation result. Figure 5.2(f) is the solution u from (3.5) using $\lambda = 1$ and $\mu = 0.5$. Notice that there is no visible noise left in u , and the bright object in the original image is smoothed out. Figures 5.2(g) and (h) are our segmentation results with thresholds $\rho^K = 92.05$ and $\rho^U = 20$ respectively. By comparing our results with the results from methods [63], [22] and [55] in Figures 5.2(c), (d) and (e) respectively, we see that our method can segment the noisy image successfully with both ρ^K and ρ^U and different meaningful details are revealed. The method [63] produced a result similar to our segmentation with threshold ρ^K , while the methods [22, 55] produced results with holes inside the bright object.

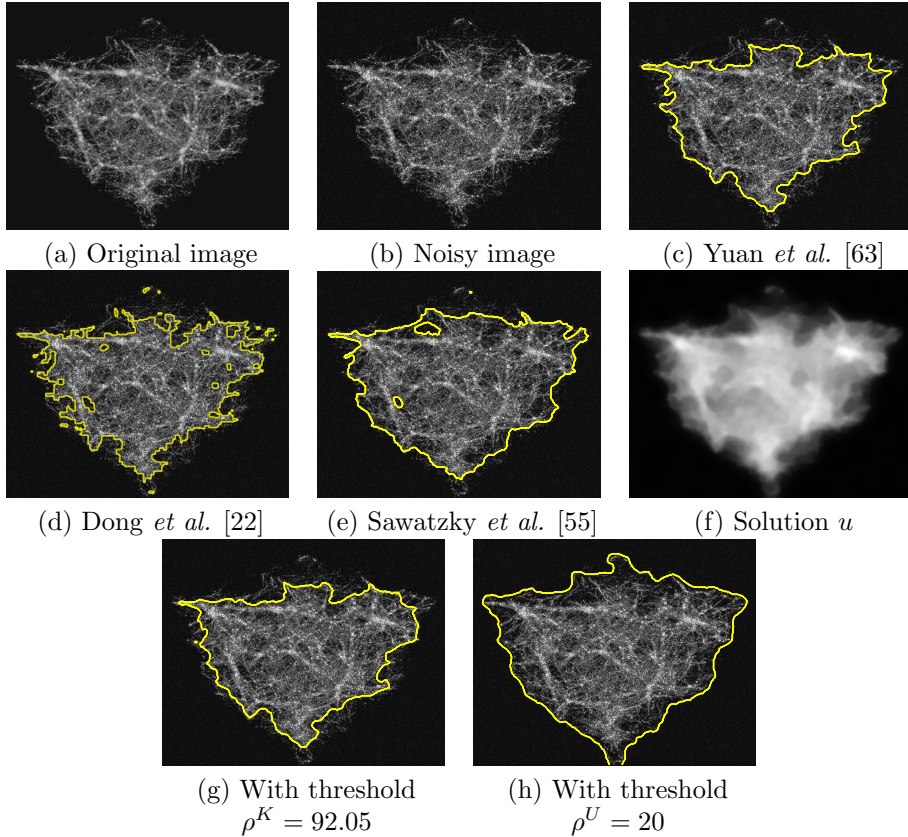


FIG. 5.2. (a) Original “Anti-mass” image (384 × 480 pixels), (b) image corrupted by multiplicative Gamma noise with $K = 10$, (c) Yuan *et al.* [63], (d) Dong *et al.* [22], (e) Sawatzky *et al.* [55], (f) solution u from (3.5) with $\lambda = 1$ and $\mu = 0.5$, (g) u with threshold $\rho^K = 92.05$, (h) u with threshold $\rho^U = 20$.

Example 5.3 (Blocky blurry image with Poisson noise): Figure 5.3(a) is the synthetic image “Shape” which has three clearly separated objects. We first blur it by a vertical motion kernel with length 31 and then corrupt it by Poisson noise, see Figure 5.3(b). The boundaries of the objects are now blurry and vague so that they are hard to detect. Figure 5.3(f) is the solution u from (3.5) using $\lambda = 15$ and $\mu = 0.001$. Figures 5.3(g) is our segmentation result with threshold $\rho^K = 129.94$. It is clear that both the blur and the noise are reduced in u , and this facilitated the detection of the separate objects. The method [63] produced a result in Figure 5.3(c) with over-

smoothed boundaries. Because of the blur, Figure 5.3(d) from the method in [22] presents distortion (see the annulus). Method [55] in Figure 5.3(e) failed to segment the three separated objects.

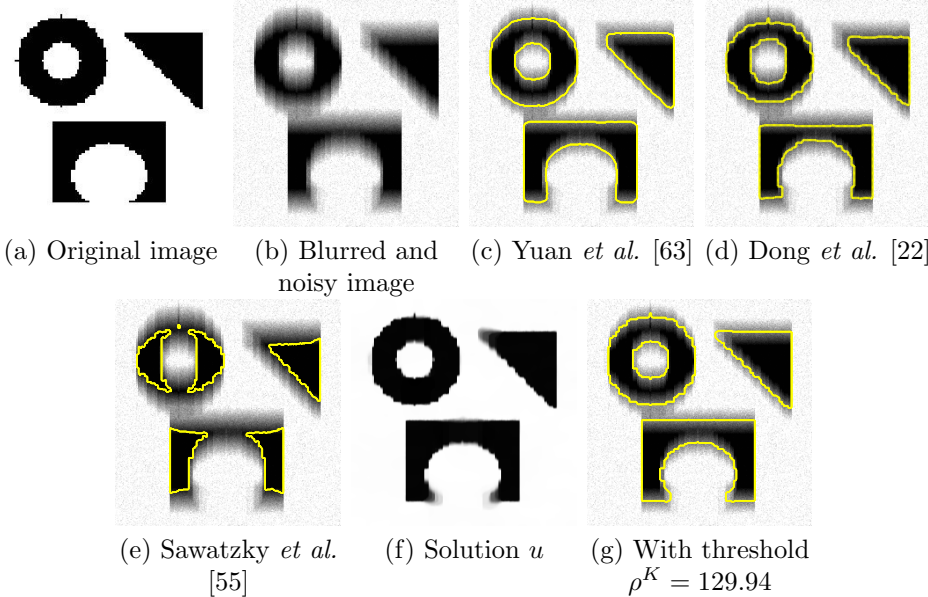


FIG. 5.3. (a) Original “Shape” image (258×256 pixels), (b) blurred image (vertical motion kernel with length 21) with Poisson noise, (c) Yuan *et al.* [63], (d) Dong *et al.* [22], (e) Sawatzky *et al.* [55], (f) solution u from (3.5) with $\lambda = 15$ and $\mu = 0.001$, (g) u threshold with $\rho^K = 129.94$.

Example 5.4 (Tubular blurry image with Gamma noise): Figure 5.4(a) is the synthetic tubular image “Tree” which resembles a fractal with lots of fine structures. We first blur it by a Gaussian kernel (size 15×15 and standard deviation 3), and then degrade it with multiplicative Gamma noise with $K = 10$, see Figure 5.4(b). Figure 5.4(f) is the solution u from (3.5) using $\lambda = 10$ and $\mu = 0.001$. Figures 5.4(g) and (h) are our segmentation results with thresholds $\rho^K = 48.94$ and $\rho^U = 14$ respectively. Comparing to the methods [63], [22] and [55] in Figures 5.4(c), (d) and (e) respectively, it is clear that our segmentation method with $\rho^U = 14$ produced a very good result. The methods [22], [55] and our method with ρ^K failed to detect fine details of the tree. Because of the blur, the method [63] produced a very coarse boundary. See Figure 5.4(i)–(l) for a detailed comparison.

Since we can easily obtain the ground truth of Figure 5.3(a) and Figure 5.4(a), in Table 5.1 we compare the percentage of correct pixels of the segmented binary images. Let the image size be $m \times n$, and the number of correct pixels segmented be N . Then the percentage of correct pixels of the segmented image is computed as $\frac{N}{mn}$. We see that our method gives the most accurate segmentation.

Example 5.5 (Real cell image): The noisy image “Cells” in Figure 5.5(a) is a real image from an automated cell tracking system [6] where the authors developed a system to track cell lineage during *Caenorhabditis elegans* embryogenesis under low exposure of lights. In their experiments, noise in the images led to false positives in nuclear identification. Here, we aim to segment all the cells in the noisy image Figure 5.5(a). The segmentation result will be useful for further processing, e.g. to locate the cells by Circular Hough Transform [49]. Figure 5.5(e) is the u from (3.5)

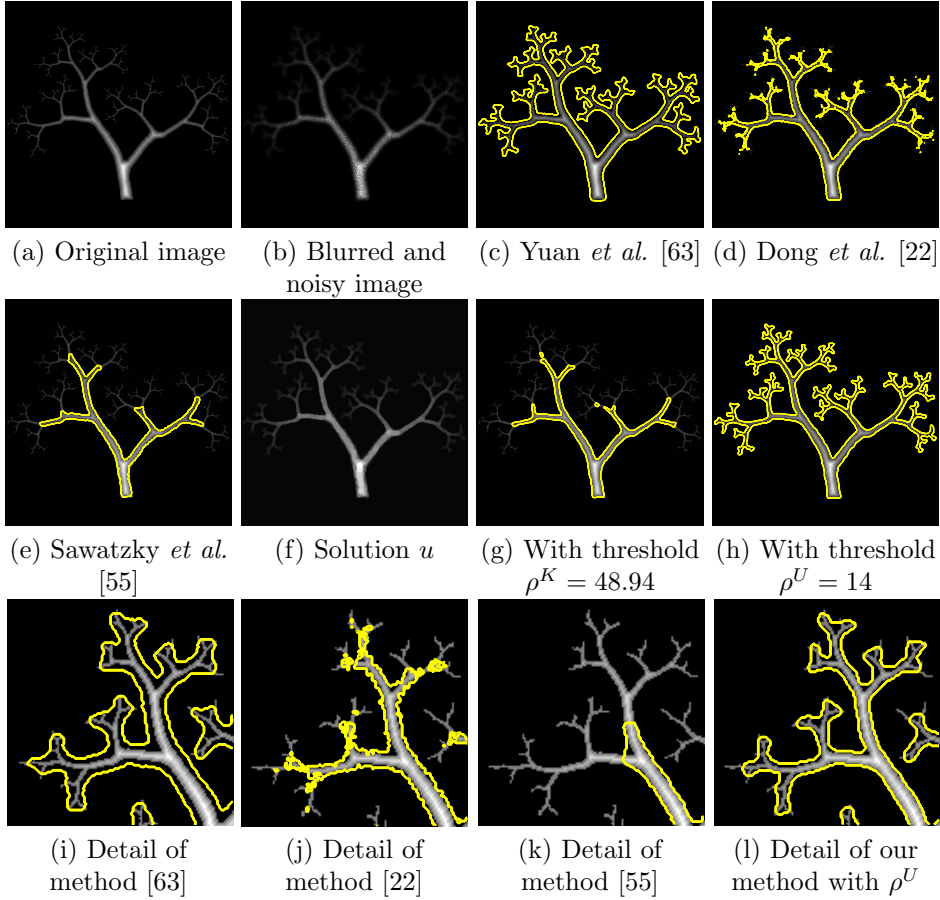


FIG. 5.4. (a) Original “Tree” image (512×512 pixels), (b) blurred image (Gaussian kernel, standard deviation 3, size 15×15) and multiplicative Gamma noise with $K = 10$, (c) Yuan et al. [63], (d) Dong et al. [22], (e) Sawatzky et al. [55], (f) solution u from (3.5) with $\lambda = 10$ and $\mu = 0.001$, (g) u threshold by $\rho^K = 48.94$, (h) u threshold by $\rho^U = 14$, (i) detail of method [63], (j) detail of method [22], (k) detail of method [55] (l) detail of our method with ρ^U .

TABLE 5.1
Percentage of correct pixels segmented for 2-phase segmentation.

	Yuan et al. [63]	Dong et al. [22]	Sawatzky et al. [55]	Our method	
Figure 5.3	98.64%	94.37%	85.22%	ρ^K	99.72%
Figure 5.4	93.10%	96.86%	96.31%	ρ^K	96.40%
				ρ^U	97.08%

using $\lambda = 10$ and $\mu = 5$. Figures 5.5(f) is our segmentation result with thresholds $\rho^K = 55.09$. Figure 5.5(g)–(i) are our segmentation results with $\rho^U = 75, 85, 95$ respectively with the same u . We stress that by changing the threshold, we do not need to re-compute u . It is clear that our threshold with ρ^K can segment almost all the cells in the noisy image, while our segment with ρ^U can get more separated cells with increasing thresholds, all with smooth boundaries. For the method [63], the cells are not separated well. For the method [22], some cells are left outside the

segmented region, and the boundaries present artificial oscillations. For the method [55], many cells are left outside the segmented region, while some segmented cells are not separated well.

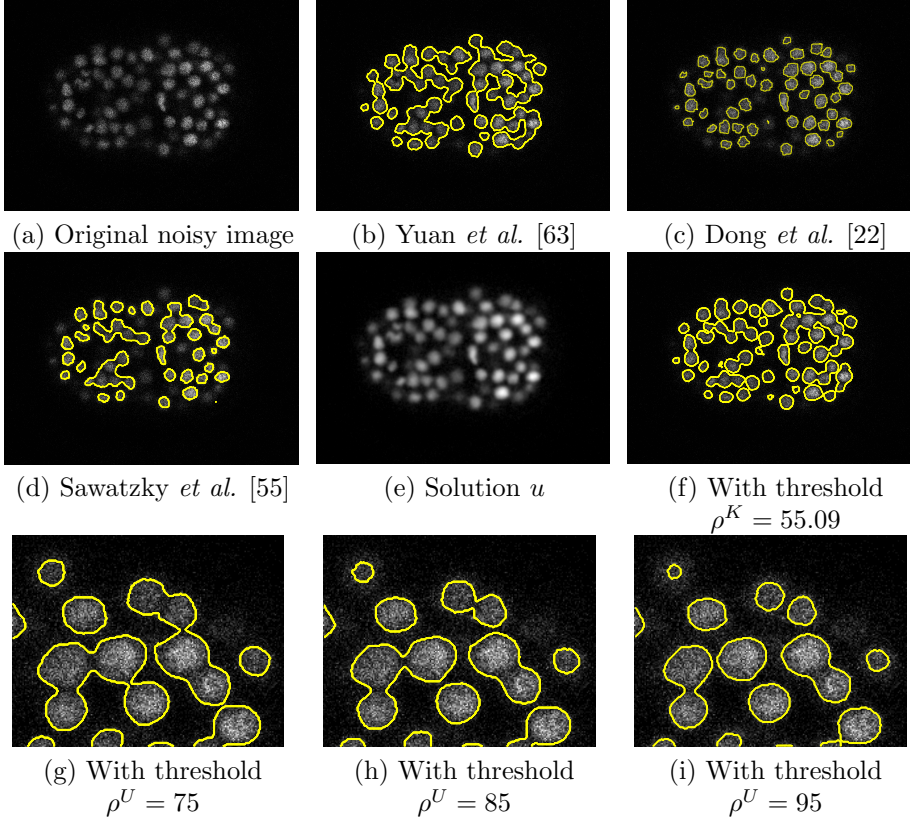


FIG. 5.5. (a) Original “Cells” image (512×712 pixels), (b) Yuan et al. [63], (c) Dong et al. [22], (d) Sawatzky et al. [55], (e) solution u from (3.5) with $\lambda = 10$ and $\mu = 5$, (f) u threshold with $\rho^K = 55.09$, (g)–(i) u threshold with $\rho^U = 75, 85, 95$ respectively.

Example 5.6 (Real bacteria image): The real “Bacteria” image has intensity only in $[0, 48]$, for better visualization we linearly stretched the image to the range $[1, 255]$. The resulting image is depicted in Figure 5.6(a) where one can see that the object in the image has high level of noise, and the boundary is vague. All the methods we tested are implemented on this linearly-stretched image. Figure 5.6(e) is the solution u from (3.5) using $\lambda = 1$ and $\mu = 1$. Figures 5.6(f) and (g) are our segmentation results with thresholds $\rho^K = 88.34$ and $\rho^U = 50$ respectively. By comparing our results with the results from methods [63], [22] and [55] in Figures 5.6 (b)–(d), we see that our segmentation with $\rho^U = 50$ produced a boundary that separates the cell from the background successfully. For the two methods [63, 22], the boundaries of the segmented regions are not smooth. Method [55] over estimated the region of interest.

In Table 5.2, we give the iteration numbers and CPU time in seconds for our method and the methods [22, 55, 63] tested above. The codes for all the methods, including ours, are written in .mat files. It can be seen that except for the deblurring cases (Figures 5.3 and 5.4), our algorithm uses the least time. The extra time in deblurring cases is justified by the good visual results and higher percentage of correctly

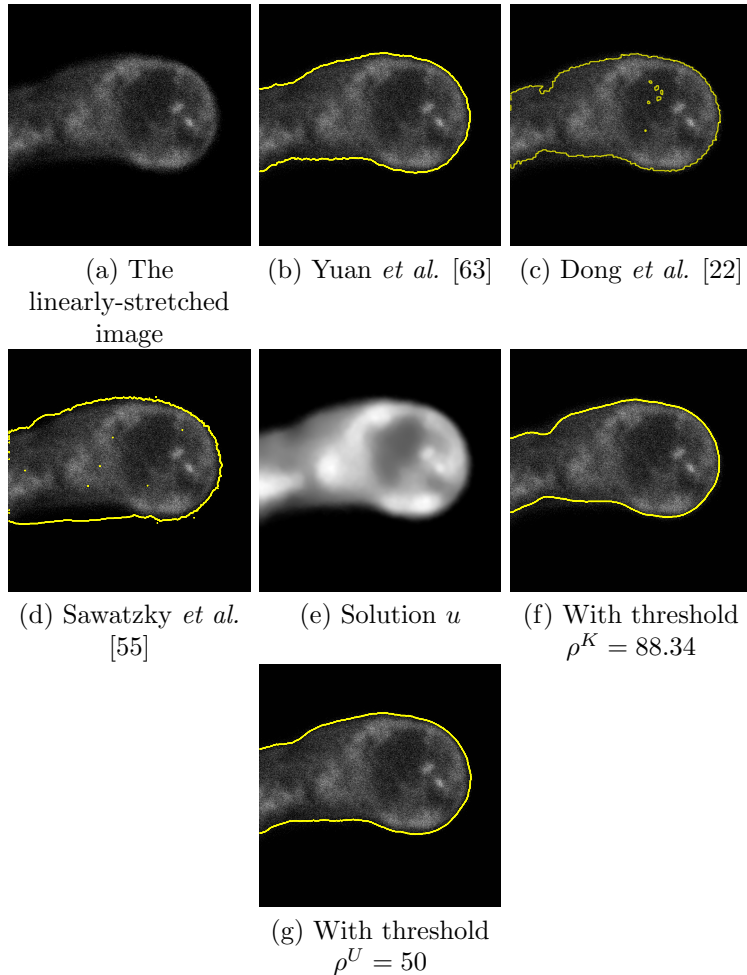


FIG. 5.6. (a) Original “Bacteria” image after linear stretching (512×512 pixels), (b) Yuan et al. [63], (c) Dong et al. [22], (d) Sawatzky et al. [55], (e) solution u from (3.5) with $\lambda = 1$ and $\mu = 1$, (f) u threshold with $\rho^K = 88.34$, (g) u threshold with $\rho^U = 50$.

segmented pixels, see Table 5.1.

5.2. Multi-phase segmentation. In this section, we compare our method with the multi-phase segmentation methods in [62] and [39].

Example 5.7 (Multiplicative Gamma noise): Figure 5.7(a) is the original “Aircraft” image and we corrupt it by multiplicative Gamma noise with $K = 10$ to get Figure 5.7(b). Figure 5.7(e) is the solution u from (3.5) using $\lambda = 2$ and $\mu = 0.01$. It is clear that our solution u is free of noise, and the cloud is smoothed out. Figure 5.7(f) is our segmentation result with thresholds $\rho^K = (48.69, 145.93)$, and Figures 5.7(g)–(i) are the three different phases we segmented. In Figure 5.7(c) from the method in [62], the cloud is not segmented as a whole. In Figure 5.7(d) from the method in [39], although we used the Anscombe transformation, noise is still visible in the segmented image.

Example 5.8 (Poisson noise): Figure 5.8(a) is the original “Shape 2” image, and we corrupt it by Poisson noise to get Figure 5.8(b). Figure 5.8(e) is the solution u

TABLE 5.2
Iteration numbers and CPU time in seconds for two-phase segmentation.

	Yuan <i>et al.</i> [63]		Dong <i>et al.</i> [22]		Sawatzky <i>et al.</i> [55]		Our method	
Example	iter.	time	iter.	time	iter.	time	iter.	time
Figure 5.1	78	3.29	187	12.66	13	324.52	61	1.52
Figure 5.2	74	5.32	239	19.51	25	562.77	80	3.19
Figure 5.3	25	0.24	66	1.95	19	152.04	325	4.12
Figure 5.4	31	3.76	295	37.13	25	1220.27	263	18.88
Figure 5.5	41	7.01	300	50.47	25	2478.45	101	6.26
Figure 5.6	51	6.33	300	36.08	25	1435.72	74	3.88

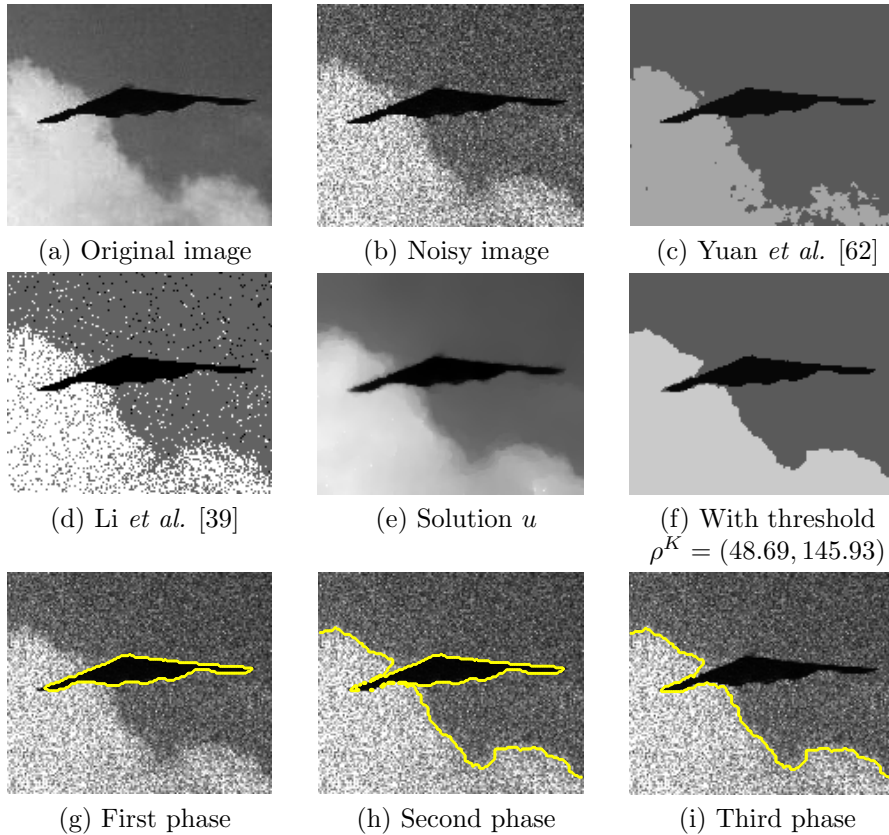


FIG. 5.7. (a) Original ‘‘Aircraft’’ image (125×150 pixels), (b) image corrupted by multiplicative Gamma noise with $K = 10$, (c) Yuan *et al.* [62], (d) Li *et al.* [39], (e) solution u from (3.5) with $\lambda = 2$ and $\mu = 0.01$, (f) u threshold by $\rho^K = (48.69, 145.93)$, (g)–(i) three-phase segmentation of u .

from (3.5) using $\lambda = 2$ and $\mu = 0.001$. It is clear that our u is almost identical to the original image, with boundaries well preserved. Figure 5.8(f) is our segmentation result with thresholds $\rho^K = (41.77, 124.34, 206.95)$. In Figure 5.8(g) we use different colors to show the boundaries of the four phases. In Figure 5.8(c) from the method in [62], the boundaries of the triangle has oscillations. Fig 5.8 (d) from [39] produced a result almost identity to the original image.

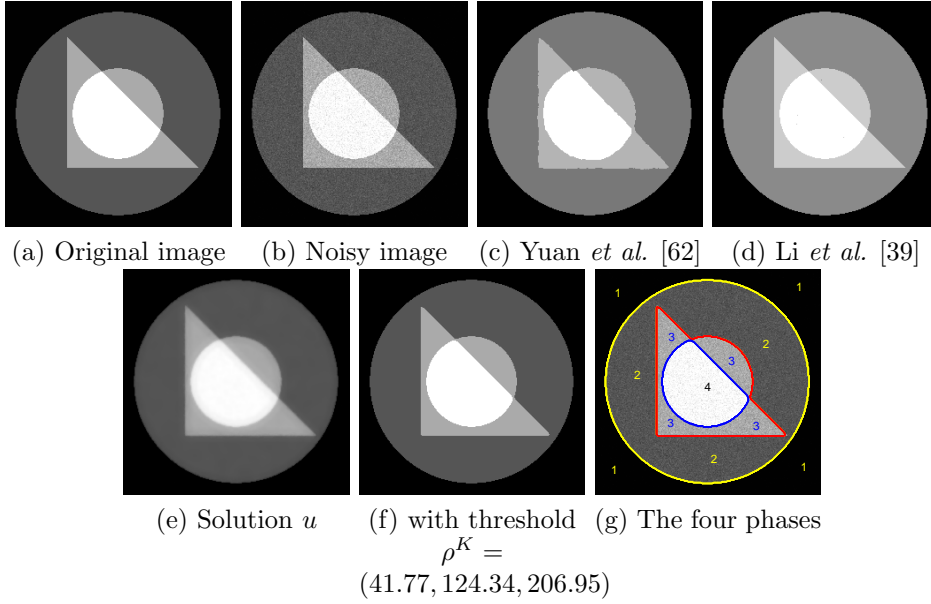


FIG. 5.8. (a) Original “Shape 2” image (256×256 pixels), (b) image corrupted by Poisson noise, (c) Yuan et al. [62], (d) Li et al. [39], (e) solution u from (3.5) with $\lambda = 2$ and $\mu = 0.001$, (f) u threshold by $\rho^K = (41.77, 124.34, 206.95)$, (g) the four different phases.

TABLE 5.3
Percentage of correct pixels segmented in 4-phase segmentation.

	Yuan et al. [63]	Li et al. [39]	Our method	
Figure 5.8	98.72%	99.99%	ρ^K	99.99%
Figure 5.9	87.03%	85.64%	ρ^K	88.59%

Example 5.9 (Blocky blurry image with Gamma noise): Figure 5.9(a) is the blurred and noisy image degraded from Figure 5.8(a); first by Gaussian kernel with standard deviation 3 and size 11 and then by multiplicative Gamma noise with $K = 20$. Figure 5.9(d) is the solution u from (3.5) using $\lambda = 2$ and $\mu = 0.001$. It is clear that our solution u is free of noise, and the blurring is significantly reduced. Figure 5.9(e) is our segmentation result with thresholds $\rho^K = (43.32, 125.01, 205.91)$, and Figure 5.9(f) shows the four different phases. Figure 5.9(b) from the method in [62] presents strong irregular oscillations on the boundaries, and Figure 5.9(c) from the method in [39] has visible noise and blurry boundaries.

Since we can easily obtain the ground truth of Figures 5.8 and 5.9, in Table 5.3 we compare the percentage of correct pixels of these segmented 4-phase images. Again, it can be seen that our method produces the best results.

Example 5.10 (Real MRI image): Finally we test the four-phase segmentation of a real MRI image, see Figure 5.10(a). Figure 5.10(d) is our solution u from (3.5) using $\lambda = 10$ and $\mu = 0.01$. Figure 5.10(e) is the segmentation of u using the thresholds $\rho^U = (110, 128, 150)$. Figures 5.10(f)–(i) are the four phases we segmented. From the images, it is clear that our method produces the best segmentation, while for methods [62] and [39], there are holes in the central bright region (marked by a red number 4 in Figure 5.10(e)).

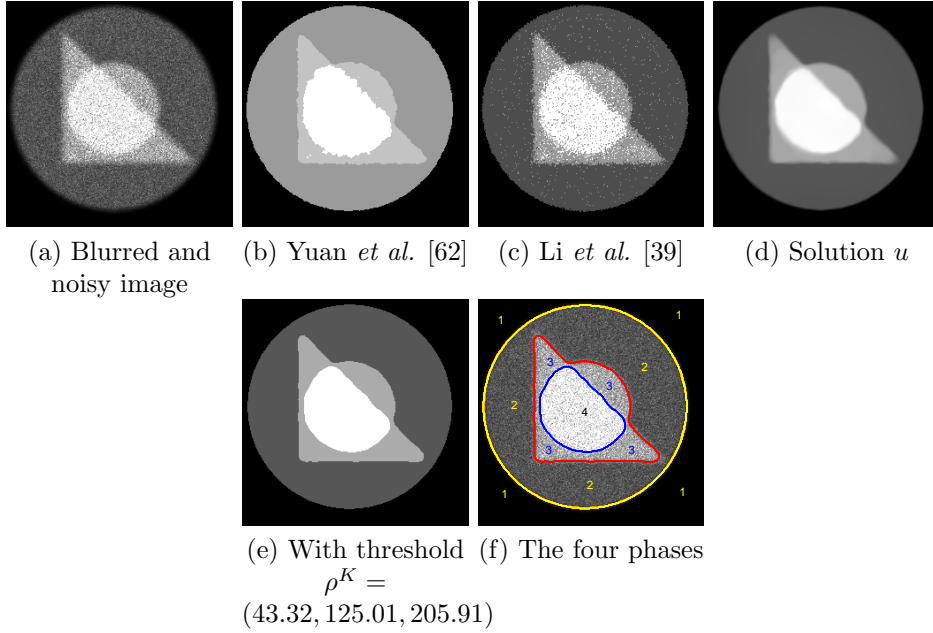


FIG. 5.9. (a) blurred and noisy image: Gaussian kernel with standard deviation 3, size 11 and multiplicative Gamma noise with $K = 20$, (b) Yuan *et al.* [62], (c) Li *et al.* [39], (d) solution u from (3.5) with $\lambda = 2$ and $\mu = 0.001$, (e) u threshold by $\rho^K = (43.32, 125.01, 205.91)$, (f) the four phases.

TABLE 5.4
Iteration numbers and CPU time in seconds for multi-phase segmentation.

	Yuan <i>et al.</i> [62]		Li <i>et al.</i> [39]		Our method	
Example	iter.	time	iter.	time	iter.	time
Figure 5.7	105	0.90	62	0.56	58	0.17
Figure 5.8	130	6.28	53	2.26	35	0.50
Figure 5.9	97	4.65	60	1.91	225	3.26
Figure 5.10	95	4.74	144	4.44	60	1.96

In Table 5.4, we give the iteration numbers and CPU time in seconds for the multi-phase segmentation we tested above. The codes for all the methods, including ours, are written in .mat files. Except for the deblurring case (Figure 5.9), our algorithm always uses the least time. Again, the extra time in deblurring is justified by the good visual results and higher percentage of correctly segmented pixels, see Table 5.3.

6. Conclusion and possible further improvements. In this paper, we have proposed a two-stage method for segmentation that makes use of a convex model (3.5). Our method has a data-fitting term related to blurring, Poisson noise and multiplicative Gamma noise. In the first stage, our method finds the unique smooth minimizer by the Chambolle-Pock algorithm. Then in the second stage, it uses thresholding strategy to segment the image. Our method combines the two-phase and multiphase segmentation into one single algorithm, and in fact one can decide the number of phases and the thresholds after the solution in (3.5) is obtained. We have employed the K-means method in Matlab to choose the thresholds automatically, or users can

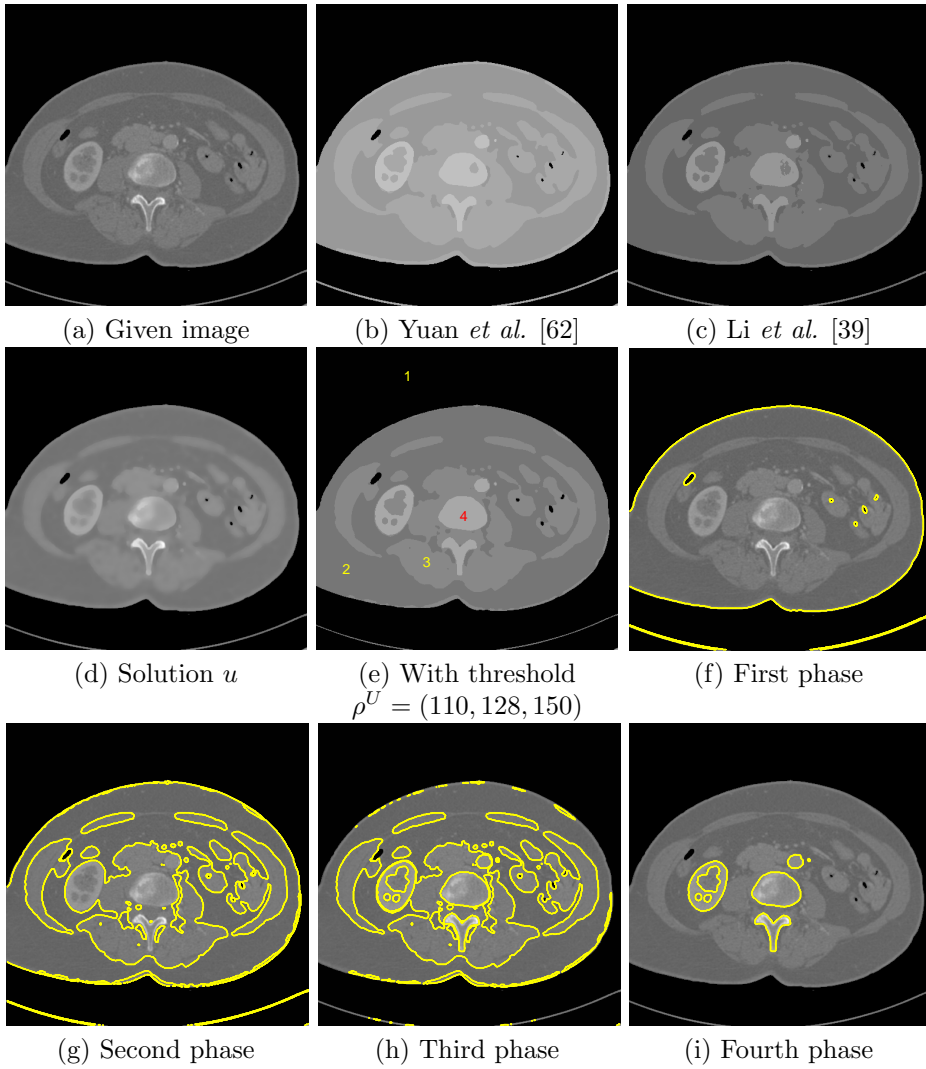


FIG. 5.10. (a) Original MRI image (512×512 pixels) (b) Yuan et al. [62], (c) Li et al. [39], (d) solution u from (3.5) with $\lambda = 10$ and $\mu = 0.01$, (e) u threshold by $\rho^U = (110, 128, 150)$, (f)–(i) the four phases.

also easily alter the thresholds without recalculating the solution in model (3.5). Our numerical experiments show that our method is very effective and robust for many kinds of images, such as anti-mass, tubular, low-light, noisy, or blurry images.

Our method may be further improved in several ways. One is to employ automatic clustering algorithms other than the K-means method to find the thresholds. Another way of improvement is to include local information in the clustering process in the second stage to better distinguish different objects of interests.

REFERENCES

- [1] L. AMBROSIO AND V. TORTORELLI, *On the approximation of free discontinuity problems*, Boll. Un. Mat. Ital., 6(1992), pp. 105–123.

- [2] L. AMBROSIO AND V. TORTORELLI, *Approximation of functionals depending on jumps by elliptic functionals via Γ -convergence*, Comm. Pure Appl. Math., 43 (1990), pp. 999–1036.
- [3] F. J. ANSCOMBE, *The transformation of Poisson, binomial and negative-binomial data*, Biometrika, pp. 246–254, 1948.
- [4] G. AUBERT AND J.F. AUJOL, *A variational approach to removing multiplicative noise*, SIAM J. Appl. Math., 68(2008), pp. 925–946.
- [5] E. BAE, J. YUAN, AND X. TAI, *Simultaneous convex optimization of regions and region parameters in image segmentation models*, Dagstuhl Seminar Proceedings, Springer. 2011.
- [6] Z. BAO, J. I. MURRAY, T. BOYLE, S. L. OOI, M. J. SANDEL AND R. H. WATERSTON, *Automated cell lineage tracing in *Caenorhabditis elegans**, Proceedings of the National Academy of Sciences of the United States of America, 103(2006), pp. 2707–2712.
- [7] L. BAR, T. CHAN, G. CHUNG, M. JUNG, N. KIRYATI, R. MOHIEDDINE, N. SOCHEN, L. VESE, *Mumford and Shah model and its applications to image segmentation and image restoration*, Handbook of Mathematical Methods in Imaging, Springer-Verlag Berlin Heidelberg, 2011, pp. 1095–1157.
- [8] S. BOYD, N. PARikh, E. CHU, B. PELEATO, AND J. ECKSTEIN, *Distributed optimization and statistical learning via the alternating direction method of multipliers*, Found. and Trends Mach. Learning, 3(2010), pp. 1–122.
- [9] X. BRESSON, S. ESEDOGLU, P. VANDERGHEYNST, J. THIRAN, AND S. OSHER, *Fast global minimization of the active contour/snake model*, J. Math. Imaging Vision, 28(2007), pp. 151–167.
- [10] E. BROWN, T. CHAN, AND X. BRESSON, *A convex relaxation method for a class of vector-valued minimization problems with applications to Mumford-Shah segmentation*, UCLA CAM Report 10–43, 2010.
- [11] X. CAI, R. CHAN AND T. ZENG, *A two-stage image segmentation method using a convex variant of the Mumford-Shah model and thresholding*, SIAM J. Imaging Sci., 6(1), 368–390.
- [12] A. CHAMBOLLE, *An algorithm for total variation minimization and applications*, J. MATH. IMAGING. VIS., 20(2004), pp. 89–97.
- [13] A. CHAMBOLLE, *Finite differences discretization of the Mumford-Shah functional*, Math. Model. Numer. Anal., 33(1999), pp. 261–288.
- [14] A. CHAMBOLLE, *Image segmentation by variational methods: Mumford and Shah functional and the discrete approximations*, SIAM J. Appl. Math., 55(1995), pp. 827–863.
- [15] A. CHAMBOLLE AND G. DALMASO, *Discrete approximation of the Mumford-Shah functional in dimension two*, Math. Model. Numer. Anal., 33(1999), pp. 651–672.
- [16] A. CHAMBOLLE AND T. POCK, *A first-order primal-dual algorithm for convex problems with applications to imaging*, J. Math. Imaging Vis., 40(2011), pp. 120–145.
- [17] T. CHAN, S. ESEDOGLU, AND M. NIKOLOVA, *Algorithms for finding global minimizers of image segmentation and denoising models*, SIAM J. Appl. Math., 66(2006), pp. 1632–1648.
- [18] T.F. CHAN, G.H. GOLUB AND P. MULET, *A nonlinear primal dual method for total variation based image restoration*, SIAM J. Sci. Comput., 20(1999), pp. 1964–1977.
- [19] T. CHAN AND L.A. VESE, *Active contours without edges*, IEEE Trans. Image Process., 10(2001), pp. 266–277.
- [20] C. CHESNAUD, P. RÉFRÉGIER AND V. BOULET, *Statistical region snake-based segmentation adapted to different physical noise models*, IEEE Trans. Pattern Anal. Mach. Intell. 21.11(1999), pp. 1145–1157.
- [21] G. DAVID, *Singular sets of minimizers for the Mumford-Shah functional (Progress in Mathematics)*, Birkhäuser Verlag, Basel, 2005.
- [22] B. DONG, A. CHIEN, AND Z. SHEN, *Frame based segmentation for medical images*, Communications in Mathematical Sciences, 2010, 9(2), pp. 551–559.
- [23] I. EKELAND, AND R. TÉMAM, *Convex Analysis and Variational Problems*, Classics in Applied Mathematics, SIAM 1999.
- [24] S. DURAND, J. FADILI, AND M. NIKOLOVA, *Multiplicative noise removal using l_1 fidelity on frame coefficients*, J. Math. Imaging Vis., 36(2010), pp. :201–226, .
- [25] S. ESEDOGLU AND Y. TSAI, *Threshold dynamics for the piecewise constant Mumford-Shah functional*, J. Comput. Phys., 211 (2006), pp. 367–384.
- [26] L. C. EVANS, *Partial differential equations*, American Mathematical Society, ISBN 0821807722, 1998.
- [27] M. FIGUEIREDO AND J. BIOCAS-DIAS, *Restoration of Poissonian images using alternating direction optimization*, IEEE Trans. Image Process., 19(2010), pp. 3133–3145.
- [28] F. GALLAND, N. BERTAUX AND P. RÉFRÉGIER, *Multi-component image segmentation in homogeneous regions based on description length minimization: application to speckle, Poisson and Bernoulli noise*, Pattern recogn. 38.11 (2005), pp. 1926–1936.

- [29] M. GOBBINO, *Finite difference approximation of the Mumford-Shah functional*, Comm. Pure Appl. Math., 51(1998), pp. 197–228.
- [30] T. GOLDSTEIN AND S. OSHER, *The split Bregman algorithm for L1 regularized problems*, SIAM J. Imaging Sci., 2(2009), pp. 323–343.
- [31] L. GRADY AND C. ALVINO, *Reformulating and optimizing the Mumford-Shah functional on a graph – a faster, lower energy solution*, European Conference on Computer Vision (ECCV), 2008, pp. 248–261.
- [32] J. HARTIGAN AND M. WANG, *A K-means clustering algorithm*, Applied Statistics, 28(1979), pp. 100–108.
- [33] M. HINTERMÜLLER AND G. STADLER, *An infeasible primal-dual algorithm for total bounded variation-based inf-convolution-type image restoration* SIAM J. Sci. Comput., 28(2006), No. 1, pp. 1–23.
- [34] T. KANUNGO, D. MOUNT, N. NETANYAHU, C. PIATKO, R. SILVERMAN, AND A. WU, *An efficient K-means clustering algorithm: analysis and implementation*, IEEE Trans. Pattern Anal. Mach. Intell., 24(2002), pp. 881–892.
- [35] Y. KIM, *Strictly convex realization in two-phase image segmentation*, UCLA CAM Report, 2013.
- [36] G. KOEPFLER, C. LOPEZ, AND J. MOREL, *A multiscale algorithm for image segmentation by variational approach*, SIAM J. Numer. Anal., 31(1994), pp. 282–299.
- [37] T. LE, R. CHARTRAND AND T. J. ASAKI, *A variational approach to reconstructing images corrupted by Poisson noise*, J. Math. Imaging Vis., 27(2007), pp. 257–263.
- [38] J. LELLMANN AND C. SCHNÖRR, *Continuous multiclass labeling approaches and algorithms*, SIAM J. Imaging Sci., 4(2011), pp. 1049–1096.
- [39] F. LI, M. NG, T. ZENG, AND C. SHEN, *A multiphase image segmentation method based on fuzzy region competition*, SIAM J. Imaging Sci., 3(2010), pp. 277–299.
- [40] F. LI, C. SHEN, AND C. LI, *Multiphase soft segmentation with total variation and H^1 regularization*, J. Math. Imaging Vision, 37(2010), pp. 98–111.
- [41] J. LIE, M. LYSAKER, AND X. TAI, *A binary level set model and some applications to Mumford-Shah image segmentation*, IEEE Trans. Image Process., 15(2006), pp. 1171–1181.
- [42] L. MA, M. NG, J. YU AND T. ZENG, *Efficient box-constrained TV-type- L^1 algorithms for restoring images with impulse noise*, Accepted to J. Comput. Math..
- [43] J. MACQUEEN, *Some methods for classification and analysis of multivariate observations*, Proc. 5th Berkeley Symposium, 1967, pp. 281–297.
- [44] M. MAKITALO AND A. FOI, *Optimal inversion of the Anscombe transformation in low-count Poisson image denoising*, IEEE Trans. Image Process., 20(2011), pp. 99–109.
- [45] P. MARTIN, P. RÉFRÉGIER, F. GOUDAIL AND F. GUÉRAULT, *Influence of the noise model on level set active contour segmentation*, IEEE Trans. Pattern Anal. Mach. Intell. 26.6 (2004), pp. 799–803.
- [46] M. MORINI AND M. NEGRI, *Mumford-Shah functional as Γ -limit of discrete Perona-Malik energies*, Math. Models and Methods in Applied Sciences, 13(2003), pp. 785–805.
- [47] D. MUMFORD AND J. SHAH, *Boundary detection by minimizing functionals*, Proceedings of IEEE conference on computer vision and pattern recognition, 1985, pp. 22–26.
- [48] D. MUMFORD AND J. SHAH, *Optimal approximations by piecewise smooth functions and associated variational problems*, Comm. Pure Appl. Math., 42(1989), pp. 577–685.
- [49] S. J. K. PEDERSEN, *Circular hough transform*, Aalborg University, Vision, Graphics, and Interactive Systems, 2007.
- [50] T. POCK, D. CREMERS, H. BISCHOF, AND A. CHAMBOLLE, *An algorithm for minimizing the Mumford-Shah functional*, Proc. 12th IEEE Int'l Conf. Computer Vision, 2009, pp. 1133–1140.
- [51] T. POCK, D. CREMERS, A. CHAMBOLLE, AND H. BISCHOF, *A convex relaxation approach for computing minimal partitions*, Proceedings of the IEEE Computer Society Conference on Computer Vision and Pattern Recognition (CVPR), 2009, pp. 810–817.
- [52] O. RUCH AND P. RÉFRÉGIER, *Minimal-complexity segmentation with a polygonal snake adapted to different optical noise models*, Optic. Lett. 26.13 (2001), pp. 977–979.
- [53] L. RUDIN, P. LIONS, AND S. OSHER, *Geometric level set methods in imaging, vision, and graphics*, chapter Multiplicative denoising and deblurring: theory and algorithms, Springer, 2003, pp. 103–119.
- [54] B. SANDBERG, S. KANG, AND T. CHAN, *Unsupervised multiphase segmentation: a phase balancing model*, IEEE Trans. Image Process., 19(2010), pp. 119–130.
- [55] A. SAWATZKY, D. TENBRINCK, X. JIANG AND M. BURGER, *A variational framework for region-based segmentation incorporating physical noise models*, J. Math. Imaging Vis., Feb., 2013, DOI: 10.1007/s10851-013-0419-6.

- [56] B. SHAFEI AND G. STEIDL, *Segmentation of images with separating layers by fuzzy c-means and convex optimization*, J. Vis. Commun. Image R., 23(2012), pp. 611–621.
- [57] J. SHI AND S. OSHER, *A nonlinear inverse scale space method for a convex multiplicative noise model*, SIAM J. Imaging Sci., 1(2008), pp. 294–321.
- [58] G. STEIDL AND T. TEUBER, *Removing multiplicative noise by Douglas-Rachford splitting methods*, J. Math. Imaging and Vis., 36(2010), pp. 168–184.
- [59] A. TSAI, A. YEZZI, AND A. WILLSKY, *Curve evolution implementation of the Mumford-Shah functional for image segmentation, denoising, interpolation, and magnification*, IEEE Trans. Image Process., 10(2001), pp. 1169–1186.
- [60] L. VESE AND T. CHAN, *A multiphase level set framework for image segmentation using the Mumford and Shah model*, Int. J. Comput. Vis., 50(2002), pp. 271–293.
- [61] J. YUAN, E. BAE, AND X. TAI, *A study on continuous max-flow and min-cut approaches*, Computer Vision and Pattern Recognition (CVPR), USA, San Francisco, 2010.
- [62] J. YUAN, E. BAE, X. TAI, AND Y. BOYCOV, *A continuous max-flow approach to Potts model*, Computer Vision-CECCV 2010. Springer Berlin Heidelberg, 2010, pp. 379–392.
- [63] J. YUAN, E. BAE, X. TAI, AND Y. BOYCOV, *A study on continuous max-flow and min-cut approaches*, Computer Vision and Pattern Recognition (CVPR), 2010 IEEE Conference on, IEEE, 2010.
- [64] J. YUAN, C. SCHNÖRR AND G. STEIDL, *Simultaneous optical flow estimation and decomposition*, SIAM J. Sci. Comput., 29(2007), pp. 2283–2304.
- [65] M. ZHU AND T. CHAN, *An efficient primal-dual hybrid gradient algorithm for total variation image restoration*, UCLA Cam report, (08-34), May 2008.